Advances in Aerodynamics

RESEARCH Open Access

Influence of the shock wave-turbulence interaction on the swirl distortion in hypersonic inlet

Zhenlong Wu[1], Yiqing Li[1*], Limei Lu[2], Xinyi Xu[1] and Ranhui Liang[1]

*Correspondence:
yiqingxmu@163.com

[1] School of Aircraft Engineering, Nanchang Hangkong University, Nanchang 330063, China
[2] Shanghai Space Propulsion Technology Research Institute, Shanghai 201112, China

Abstract

This study uses the Large Eddy Simulation (LES) technique to conduct an exhaustive analysis of the flow characteristics within the Rectangular-to-Elliptical shape Transition (REST) inlet under Mach 6 conditions. It mainly focuses on investigating the influence of the shock wave-turbulence interaction on the swirl distortion at the inlet exit. At the design condition, characterized by 0° Attack and 0° Sideslip, the incident shock wave at the inlet lip undergoes multiple reflections within the boundary layer of the domain wall, culminating in the formation of turbulent structures. The first reflected shock wave has the highest energy, exerting a significant impact on the boundary layer and the exit swirl distortion. On the contrary, the energy of the incident shock wave is progressively reduced due to repeated reflections, which results in reducing the exit swirl distortion. Under off-design conditions, characterized by 6° Attack and 0° Sideslip as well as 6° Attack with 6° Sideslip, variations in the incoming flow make the incident shock wave move inward, decreasing the frequency of shock wave reflections and even significantly reducing the reflected shock waves under conditions of 6° Attack and 6° Sideslip. However, this results in significantly increasing the exit swirl angle and distortion intensity. The obtained results demonstrate that changes in the incoming flow conditions significantly affect the level of exit swirl distortion by modulating the shock wave-turbulence interaction, especially in terms of the positioning of the incident shock wave and the quantity of reflected shock waves. In addition, this paper studies the wall heat transfer coefficient of the inlet. The obtained results show that the interaction between shock waves and the boundary layer significantly affects the heat transfer coefficient. This study provides a foundation for the comprehension and prediction of the performance of hypersonic inlets across a spectrum of flight conditions, and for the guidance of the design and optimization of such inlets.

Keywords: REST inlet, Hypersonic inlet, Large eddy simulation, Turbulence, Swirl distortion measurement

1 Introduction

The inlet system is a critical component within hypersonic vehicles, playing a crucial role in providing effective compressed gas for propulsion and engine performance [1, 2]. Smart developed and created the Rectangular-to-Elliptical Shape Transition

(REST) inlet, which is a typical three-dimensional hypersonic inlet [3–7]. Subsequent tests conducted by Smart et al. [8, 9] confirmed the utility of this fixed-geometry inlet across a spectrum of Mach numbers for ramjet engines. However, other numerical and experimental studies showed that two principal challenges are associated with the REST inlet: the presence of a highly distorted flow field and the complexities of shock wave-turbulence interactions. These phenomena can compromise the resilience of the inlet against the back pressure of the combustion chamber, resulting in many limitations including airflow separation, total pressure loss, swirling flows, and inlet start failure [10–13]. Given the emergent studies on shock wave-turbulence interactions and swirl distortion, a thorough investigation into their interconnection is essential.

The shock wave-turbulence interactions are common occurrences in hypersonic inlets, which can engender unfavorable pressure gradients, precipitating flow separation and limiting the overall performance of the vehicle. Although hypersonic flows are characterized by high-order energy interactions, the current studies on inlet shock wave boundary layer interactions mainly focus on supersonic flows, while the incorporation of direct comparisons with hypersonic flows is infeasible [14–16]. Zhang et al. [17] studied the relationship between boundary layer interactions and cowl shocks under the influence of expansion waves. Their results revealed a positive impact on the shock and boundary layer interactions, when cowl shocks affect the shoulder. Meshram et al. [18] studied blunt body double wedge hypersonic flows. They deduced that increasing the deflection angles amplifies the inverse pressure gradients stemming from shock boundary layer interactions, which results in enlarging the separated bubble region. Zahrolayali et al. [19] studied the impact of the shock wave-boundary layer interactions modulated by heat sources. They deduced that adjusting the size and power of the heat source significantly affects the shock wave formation and the subsequent interactions within the isolation section, which may lead to unstable inlet performance and ignition issues. Guo et al. [20] and Zhu et al. [21] clarified the physical processes underlying the shock boundary layer interactions and the mitigating effects of the transverse jets on the separation phenomena.

The transmission of swirl distortion through the inlet isolation section can significantly affect the fuel mixing and the combustion process within the combustion chamber. Consequently, the analysis of the outlet swirl distortion is crucial in the design of auxiliary engines. Emami et al. [22] studied the relationship between inlet chamber isolators and inlet distortion in dual-mode scramjet engines. Their results showed a correlation between the increased inlet distortion and the isolator size with the enhanced maximum back pressure capacity of the combined inlet isolator. Ombrello et al. [23] conducted experimental studies on the impact of the inlet distortion on the ignition process using a cavity-based flame holder, showing significant effects on the fuel injection mass flow rates and the spark energy required for ignition. Li et al. [24] assessed the relationship between the swirl distortion and the total outflow pressure under various inlet settings for a Busemann inlet. Their results showed significantly higher levels of total pressure distortion and swirl distortion under off-design conditions compared with design conditions. Furthermore, they deduced that the average value of pulsation distortion is greater than that of the total pressure distortion and swirl distortion.

Many studies have been conducted on the swirl distortion and shock wave-turbulence boundary layer interaction, while few addressed their combined effects or established a clear methodology for assessing the flow distortion at the exit of a hypersonic inlet. The computational fluid dynamics (CFD) methods include RANS, LES, DNS, and DES. This study employs the LES approach to numerically investigate the shock wave-turbulence interactions within turbulent flows. Note that LES is selected for its ability to accurately capture essential turbulence characteristics while managing the computational load. In addition, distortion descriptors are used to quantitatively define the swirl distortion at the inlet exit, highlighting the intrinsic relationship between shock wave-turbulence interaction and swirl distortion in hypersonic inlets.

The remainder of this paper is organized as follows. Section 2 outlines the numerical computation methods, comprising the REST inlet model, the mesh model, and the numerical simulation scheme. Section 3 presents an analysis of the time-averaged and instantaneous flow characteristics of the REST inlet under both design and off-design conditions. Section 4 details the conducted study on the vorticity within the inlet, and quantifies the swirl distortion at the exit plane using a distortion descriptor. Finally, the conclusion is drawn in Section 5.

2 Methodology

2.1 Numerical method

Using an in-house flow solver, the flow field of the REST inlet, characterized by a free-stream Mach number of 6.0, was subjected to numerical modeling under various operational conditions. The simulations were performed by employing the Large Eddy Simulation (LES) technique, which has been previously implemented and validated in [24]. The discretization of the three-dimensional compressible Navier–Stokes equations [25] was performed by applying the finite volume method. The corresponding governing equations, based on their integral form [26], are expressed as:

$$\frac{\partial}{\partial t}\int_{\Omega} W d\Omega + \oint_{\partial\Omega} (F_{inv} - F_{vis}) dS = 0, \tag{1}$$

where dS is the cell surface integral which effectively delineates the boundaries of the control volume, F_{vis} is a vector representing the viscous flow, F_{inv} is a vector representing the inviscid flux, and W is a vector comprising the conserved variables.

When employing the Roe's flux-difference splitting scheme for the discretization of the inviscid convective fluxes, the mathematical expression of F_{inv} can be written as:

$$F_{inv} = \frac{1}{2}\left(F_{R,inv} + F_{L,inv}\right) - \frac{1}{2}\Gamma\left|\hat{A}\right|\delta W. \tag{2}$$

Within the computational framework, the solution vectors W_R and W_L, representing the respective states on the right and left sides of the computational face, are employed to determine the inviscid fluxes $W_{R,inv}$ and $W_{L,inv}$. The spatial discrepancy between these states, which is denoted by δW, is equal to $W_R - W_L$. To discretize the viscous fluxes, a second-order centered difference approximation is applied. Furthermore, temporal integration is performed by employing a point implicit scheme, which is a complex method particularly suited for advanced time-stepping procedures.

The Wall-Adapting Local Eddy-Viscosity (WALE) model is used to simulate the turbulence. This model is characterized by its efficiency in characterizing the turbulent flow phenomena. The eddy-viscosity coefficient is a crucial parameter within the WALE model, which is computed as:

$$\mu_t = \rho \Delta_s^2 \frac{\left(S_{ij}^d S_{ij}^d\right)^{3/2}}{\left(\overline{S}_{ij}\overline{S}_{ij}\right)^{5/2} + \left(S_{ij}^d S_{ij}^d\right)^{5/4}}. \tag{3}$$

Note that in the sequel, x_i ($i = 1, 2, 3$) denotes the coordinates in the X, Y, and Z directions, and u_i ($i = 1, 2, 3$) denotes the corresponding velocities (u, v, and w) in these directions. The parameters of Eq. (3) are computed as:

$$\Delta_s = C_\omega V^{1/3}, \tag{4}$$

$$S_{ij}^d = \frac{1}{2}\left(\overline{g}_{ij}^2 + \overline{g}_{ji}^2\right) - \frac{1}{3}\delta_{ij}\overline{g}_{kk}^2, \tag{5}$$

$$\overline{g}_{ij} = \frac{\partial \overline{u}_i}{\partial \overline{x}_j}, \tag{6}$$

$$\overline{g}_{ij}^2 = \overline{g}_{ik}\overline{g}_{kj}. \tag{7}$$

The resolved velocity field is used to calculate the strain velocity tensor:

$$\overline{S}_{ij} = \frac{1}{2}\left(\frac{\partial \overline{u}_i}{\partial \overline{x}_j} + \frac{\partial \overline{u}_j}{\partial \overline{x}_i}\right). \tag{8}$$

In the WALE model, the model coefficient is equal to:

$$C_\omega = 0.325. \tag{9}$$

The inlet wall surface is subjected to the adiabatic wall boundary condition using the following formula:

$$q_s = -\kappa \frac{d\overline{T}}{d\overline{x}_{wall-normal}} = 0. \tag{10}$$

2.2 Computation model and grid convergence study

The Rectangular-to-Elliptical Shape Transition (REST) inlet prototype is illustrated in Fig. 1. The total length of the model (from the leading edge of the compression surface to the terminal end of the isolator) is 1305 mm. The transitional segment of the central rotating ellipse spans 694 mm, while the isolation section has a length of 434 mm. The entry of the isolation portion is characterized by an oval-shaped cross-section with major and minor axes of 120 mm and 66 mm, respectively. The free-flow capture surface has a width of 305 mm and a height of 162 mm. The internal contraction ratio of the inlet is equal to 1.63, while the overall contraction ratio is 6.58.

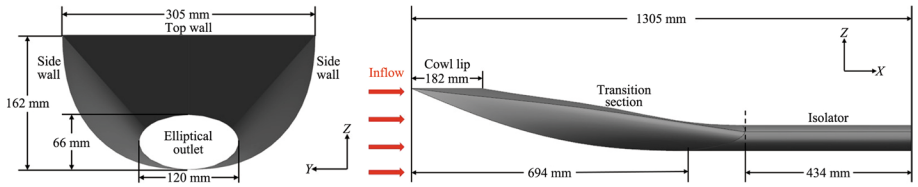

Fig. 1 Side and front views of the REST inlet model

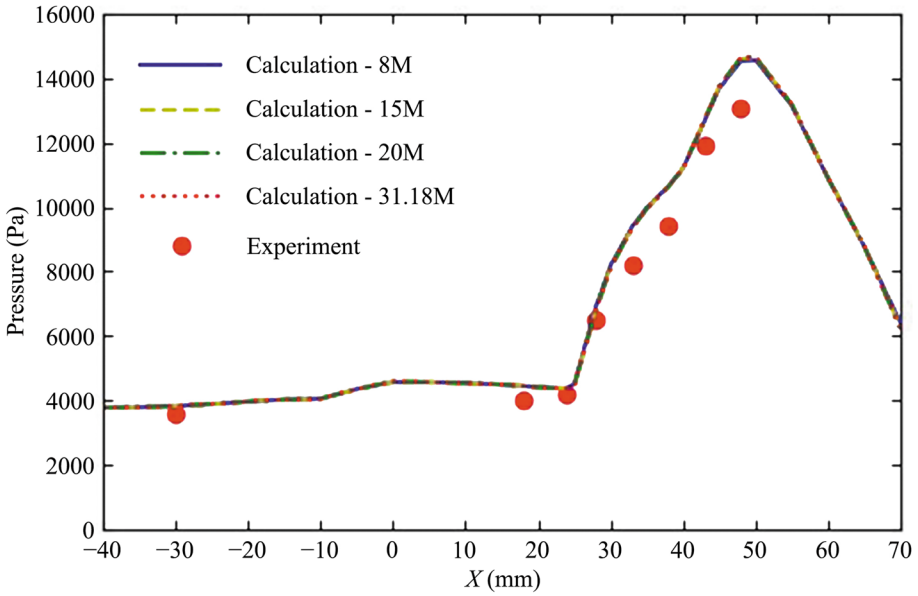

Fig. 2 Grid verification diagram

To validate the efficiency of the in-house flow solver and the employed numerical strategy, the analytical model presented in [27] was redeveloped using the methodologies outlined within this investigation. The outcomes of the computational fluid dynamics (CFD) were then compared with empirical data to verify their similarity. Figure 2 presents a comparative analysis of the pressure distributions along the spanwise centerline ($z = 25.05$ mm) of the lower wall of the model. This analysis comprises four distinct grid configurations, each having an escalating total grid count: 8, 15, 20, and 31.18 million cells, and it is complemented by corresponding experimental data. The CFD predictions result in a slight overestimation. However, they exhibit a tolerable error margin. It can be observed from Fig. 2 that the computational results for the four grid configurations converge, which demonstrates that the numerical solution achieved a state of grid independence, indicating the high robustness of the mesh resolution. The grid having 31.18 million cells was finally adopted to obtain higher resolution and provide a more detailed visualization of the boundary layer properties, shock turbulence interactions, and separation zone structure.

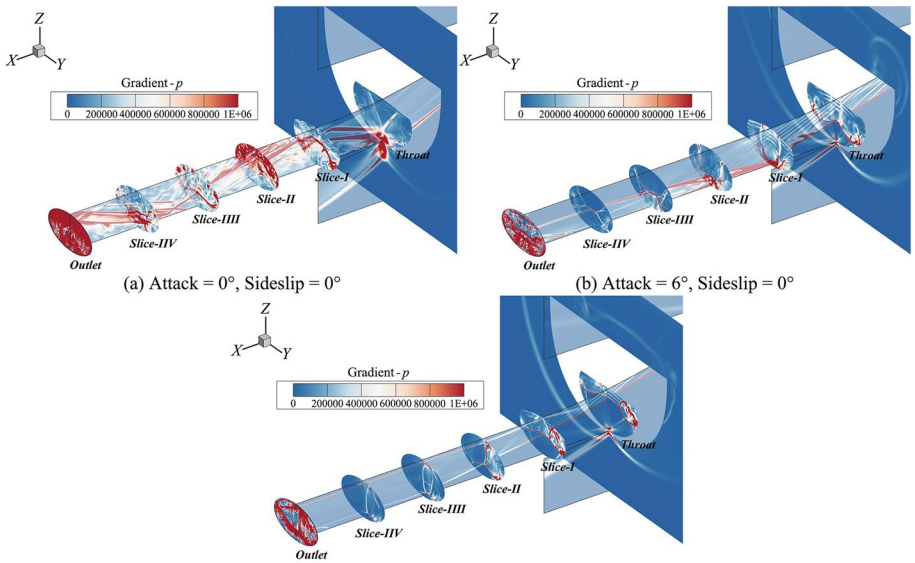

Fig. 3 Pressure gradient slice contour of the REST inlet

3 Analysis of the flow characteristics

In this section, the flow characteristics of the REST inlet are studied under three specific design conditions. The analysis is conducted on a constant set of free-stream parameters, including a temperature $T_0 = 221$ K, a static pressure $P_0 = 2549$ Pa, and a Mach number $Ma = 6$. These parameters serve as an invariant benchmark for the inflow state across all the considered scenarios. The analysis incorporates two off-design conditions, which are defined by a combination of non-zero Attack and Sideslip. The first one consists of an Attack of 0° and a Sideslip of 6°, and the second one consists of an Attack of 6° and a Sideslip of 6°. The primary divergence from the design condition is encapsulated in the non-zero values of Attack and Sideslip, which are both set to 0° at the design point.

3.1 Instantaneous flow characteristics

The pressure gradient contours (Fig. 3) are analyzed at three specific design conditions, comprising the six transverse planes from the throat to the outlet of the elliptical section and the central X–Z plane. It can be seen from Fig. 3 that, at the design condition, characterized by an Attack of 0° and a Sideslip of 0° (Fig. 3a), the incident shock wave originating from the inlet lip accurately strikes at the midpoint of the lower wall of the throat. In the subsequent Slice II, a reflected shock wave affects the upper wall, leading to the erosion of the boundary layer and the consequent formation of numerous turbulent structures. This region is considered the most unstable within the flow domain due to the elevated turbulence induced by the re-reflected shock waves. As the flow progresses through Slice III, the magnitude of the turbulent structures is reduced, yet the perturbation to the boundary layer by the shock waves remains evident. In the off-design conditions illustrated in Fig. 3b, the incident shock wave further advances into the inlet port as a result of the changes in the Attack of the incoming flow. The turbulent boundary layer is mainly situated between Slices I and II, and it reattaches between Slices II

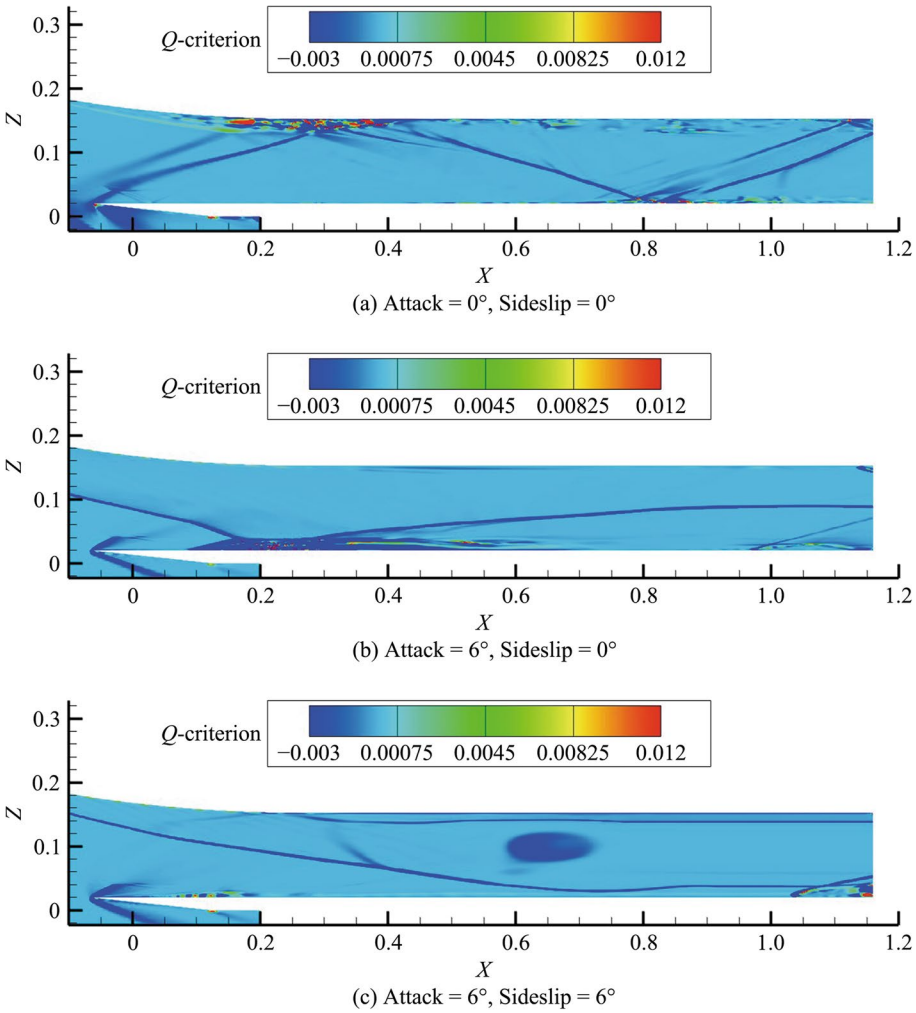

Fig. 4 The contours of *Q* criterion of the REST inlet symmetry surface

and III. Figure 3c presents the asymmetry that arises in the flow when both the Sideslip and the Attack are non-zero, while the shock wave and boundary layer interactions contribute to this deviation, affecting the upper wall on the right side of the inlet port. Deep comprehension of the characteristics and performance of the flow, emphasizing its transient nature within the inlet, is usually reached using the pressure gradient as a metric. Consequently, a systematic analysis based on the pressure gradient is essential for a thorough understanding of the inlet flow dynamics.

Figure 4 shows the contours of the Q criterion of the REST inlet symmetry surface, allowing to more clearly observe the turbulence and vortex structure. It is defined as:

$$Q = \frac{1}{2}\left(\tilde{\Omega}_{ij}\tilde{\Omega}_{ij} - \tilde{S}_{ij}\tilde{S}_{ij}\right), \tag{11}$$

where $\tilde{S}_{ij} = \frac{1}{2}\left(\frac{\partial \tilde{u}_i}{\partial x_j} + \frac{\partial \tilde{u}_j}{\partial x_i}\right)$ and $\tilde{\Omega}_{ij} = \frac{1}{2}\left(\frac{\partial \overline{u}_i}{\partial x_j} - \frac{\partial \overline{u}_j}{\partial x_i}\right)$ represent the symmetric and antisymmetric parts of the velocity gradient tensor, respectively.

For the region defined by $Q>0$, the rotation rate of the fluid is greater than the strain rate, and the flow vortex structure is dominant. It can be seen from Fig. 4a and b that the regions with $Q>0$ are mainly concentrated in the shock wave-boundary layer, where strong turbulent activity exists on the surface, and boundary layer separation and reattachment can also be found. However, for 6° Attack and 6° Sideslip, the distribution of the Q criterion shows a negative value without clear turbulent structure. This may be due to the asymmetric flow field caused by the introduction of Sideslip, and the migration of the area with $Q>0$ to the side wall of the inlet port, which is also consistent with the analysis in Fig. 3c.

Figure 5 presents the contours of the instantaneous swirl angle and the instantaneous total pressure at the inlet–outlet interface, highlighting the airflow characteristics within the inlet. In order to normalize the data, the incoming flow properties are employed to render the total pressure dimensionless, while the maximum swirl angle observed at the outlet plane is used to non-dimensionalize the swirl angle. The swirl angle is computed as:

$$\alpha = \tan^{-1}\left(\frac{U_\theta}{U_x}\right), \tag{12}$$

where U_θ and U_x denote the circumferential and axial components of the velocity vector, respectively.

It can be seen from Fig. 5 that the instantaneous total pressure contours allow to clearly observe the turbulent structures proximal to the inlet–outlet boundary layer at Attack and Sideslip of 0°. The regions of low total pressure are predominantly localized within these turbulent boundary layers. The swirl angle contours indicate the presence of two distinct regions with positive and negative swirl angles, albeit with minimal magnitudes. In the non-design condition illustrated in Fig. 5c, the boundary layer thickness increases while the turbulent structure of the outlet decreases. In addition, it can be seen from Fig. 5e that the area of low pressure at the outlet plane expands when the incoming flow is subjected to a Sideslip. This expansion is due to the formation of a turbulent boundary layer over a short distance, which then fails to reattach. This phenomenon occurs as the incident shock wave at the lip progresses inward, trailing the point of the boundary layer interference. In the case where the incoming flow is characterized solely by the Angle (Fig. 5d), the positive and negative swirl angle regions at the outlet plane are extended, surrounding a central swirl pair. Furthermore, when both the Attack and the Sideslip are applied to the inflow, the region of negative swirl angle dominates the outlet plane, which closely mirrors the distribution of the boundary layer observed in the overall pressure contours. It can then be deduced that turbulence exists even at the design point. The introduction of a turbulent boundary layer, precipitated by variations in the Attack and Sideslip, results in extending the low-pressure region at the outlet plane, the swirl distribution area, and the swirl angle in the vicinity of the wall. This can result in a significant total pressure loss within the inlet.

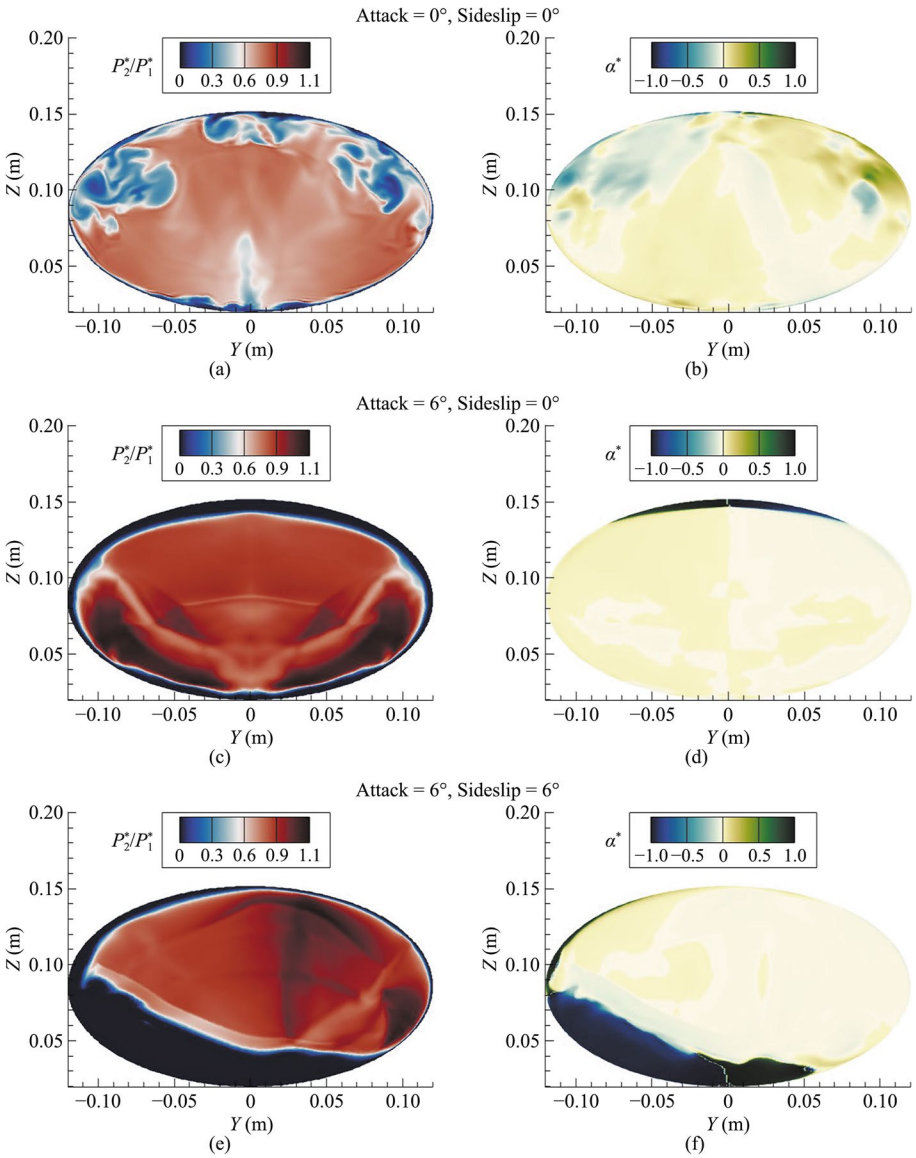

Fig. 5 The instantaneous total pressure and instantaneous swirl angle contours of the REST inlet outlet

This section employs numerical simulations to study the transient flow characteristics of the REST inlet at various design and off-design conditions. Figure 3 presents the pressure gradient slice contours, which highlight the influence of the shock wave-boundary layer interactions on the flow structure, with a particular emphasis on the differences observed between the design and off-design points. Figure 4 illustrates the distribution of turbulence and vortex structures through the Q criterion iso-contours, as well as their relationship with the shock wave-boundary layer interactions. Figure 5 shows the instantaneous swirl angle and total pressure iso-contours, allowing to analyze the details of the internal airflow within the inlet, as well as the impact of these flow characteristics on its performance. These analyses underscore the significance of comprehending the

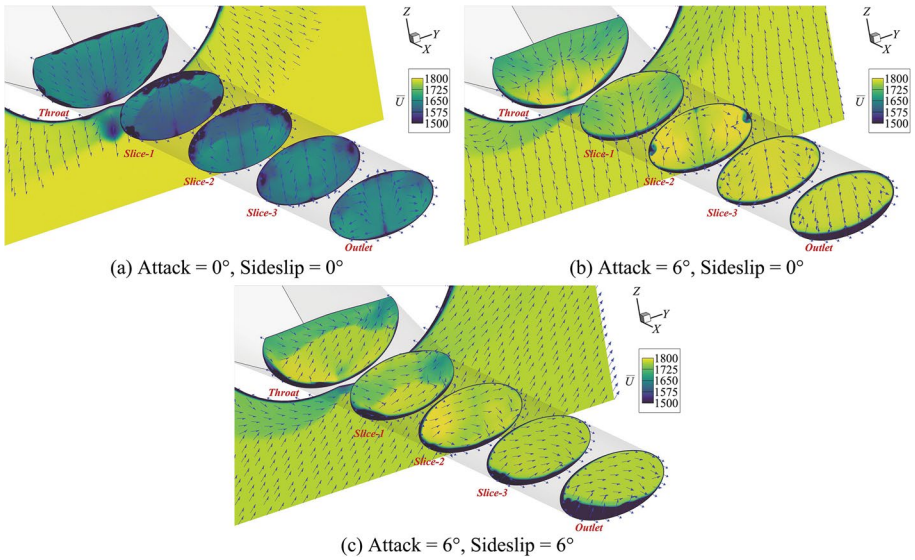

Fig. 6 The time-averaged velocity distribution slice contour and velocity vector of the REST inlet

transient flow characteristics of hypersonic inlets during the design phase, as it is crucial for optimizing the design, enhancing the performance, and ensuring high reliability.

3.2 Time-averaged flow characteristics

Figure 6 presents the contours of the time-averaged velocity distribution and the velocity vector in a cross-sectional slice of the REST inlet. Note that the focus is only on the cross-sectional contour, as the flow characteristics from the transition section to the outlet plane are of primary interest. The cross-sectional velocity vector contour is derived from the combination of time-averaged velocity vectors aligned in the y and z directions. The contour representing the time-averaged velocity distribution corresponds to the mean velocity in the x direction. At the underlying design condition (i.e., both the Attack and the Sideslip are set to 0°), the overall time-averaged velocity within the inlet port is lower than that at the non-design condition, as shown in Fig. 6a. The region of low velocity is mainly located along the upper wall and the sidewalls of the inlet. The velocity vector, while dispersed along the plane from the inlet to the outlet, exhibits a distinct vortex structure. On the contrary, within the throat, the velocity vector is uniformly distributed, and it converges towards the central region of the descending wall. At the non-design condition with a Sideslip of 0° and an Attack of 6°, the velocity in the x direction, with the exception of the boundary layer at the bottom, is mainly sustained at a higher level and uniformly distributed, as shown in Fig. 6b. At the throat, the velocity vector converges in the center, mirroring the pattern observed in Fig. 6a. This may be attributed to the inward migration of the shock waves due to the increased Attack. The distribution of the velocity vector across slices 2 and 3, as well as the outlet plane, indicates that the flow separation along the lower wall results in a thickened boundary layer at the outlet plane. Furthermore, the disturbance induced by the shock wave in the anterior section of the inlet to the boundary layer perturbs the flow in the posterior section, which allows the generation of a vortex. When both the Sideslip and the Attack are increased to 6°,

the velocity vector shifts to the right under the synergistic action of the Attack and Sideslip, intensifying the interference of the shock waves on the boundary layer, as shown in Fig. 6c. The left lower wall is identified as the primary region where the boundary layer accumulates and thickens.

The wall heat transfer coefficient is a critical parameter for evaluating the impact of aerodynamic heating on the inlet wall. In engineering applications, the time-averaged heat transfer coefficient is mostly used, as it provides a more accurate representation of the overall heat transfer performance. Figure 7 presents the heat transfer coefficient contour maps for the upper and lower walls of the REST inlet under various conditions, as well as the variation of the heat transfer coefficient at the centerline of the upper and lower walls. It can be seen from Fig. 7a that for Attack and Sideslip of 0°, the boundary layer disturbance induced by the incident shock wave is enhanced, despite the fact that the shock wave does not directly affect the lower wall. Observations from the upper wall reveal the emergence of numerous banded turbulent structures in the boundary layer under the influence of the reflected shock wave, which results in significantly increasing the heat transfer coefficient within the region of shock-boundary layer interaction. When the Attack increases to 6° (Fig. 7b), the inward shift of the incident shock wave leads to the distinct visualization of extensive turbulent structures on the lower wall. In addition, the direct interaction point between the shock wave and the boundary layer causes a peak in the heat transfer coefficient on the wall surface. On the contrary, no significant turbulent structures are observed on the upper wall, which is consistent with the results presented in Fig. 6b. When the Attack and the Sideslip simultaneously change (Fig. 7c), the flow exhibits a pronounced asymmetry. The Sideslip makes the shock-turbulence interaction mainly concentrated on the side walls. However, peak points of the heat transfer coefficient still appear on the lower wall, although their magnitude is less pronounced compared with the case incorporating only the variation of the Attack.

Numerical simulations are then performed to study the time-averaged flow characteristics of the REST inlet at design and off-design conditions. Figure 6 presents the time-averaged velocity distribution and velocity vector contours of the inlet, highlighting the flow characteristics from the transition section to the outlet plane. When the Attack and the Sideslip are equal to zero, the overall time-averaged velocity is lower, and the velocity vectors are uniformly distributed and converge in the throat region. On the contrary, at off-design points, the velocity vector distribution is asymmetric, and the interaction between the shock waves and the boundary layer results in the emergence of peak heat transfer coefficients. Figure 7 illustrates the heat transfer coefficient contours for the upper and lower walls, as well as the variation of the heat transfer coefficient at the centerline, indicating the influence of the boundary layer disturbance enhancement and shock wave-boundary layer interaction on the heat transfer coefficient. The results analyzed in this section demonstrate the significance of thoroughly understanding the time-averaged flow characteristics of the inlet during the design process, as it is crucial for performing performance optimization and ensuring high reliability.

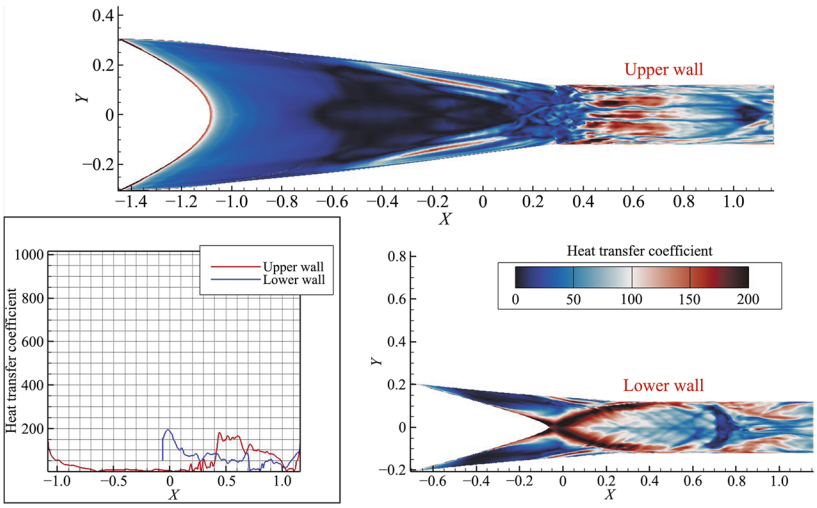

(a) Attack = 0°, Sideslip = 0°

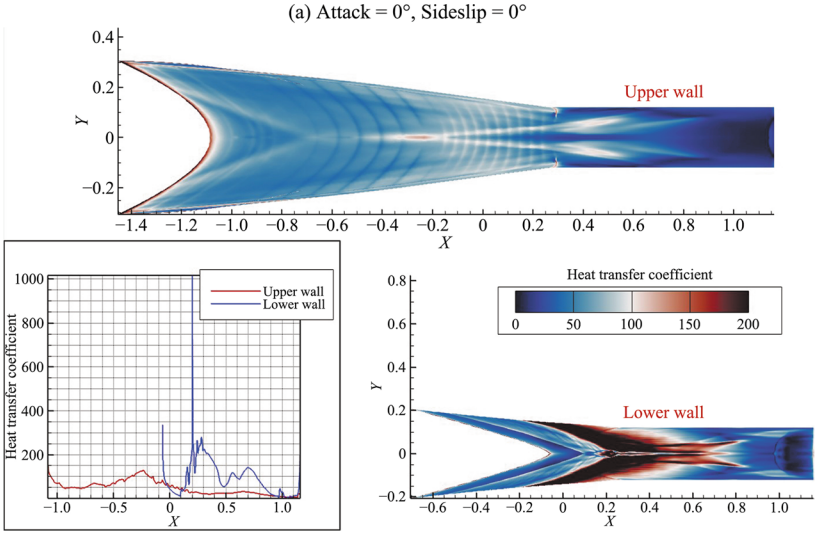

(b) Attack = 6°, Sideslip = 0°

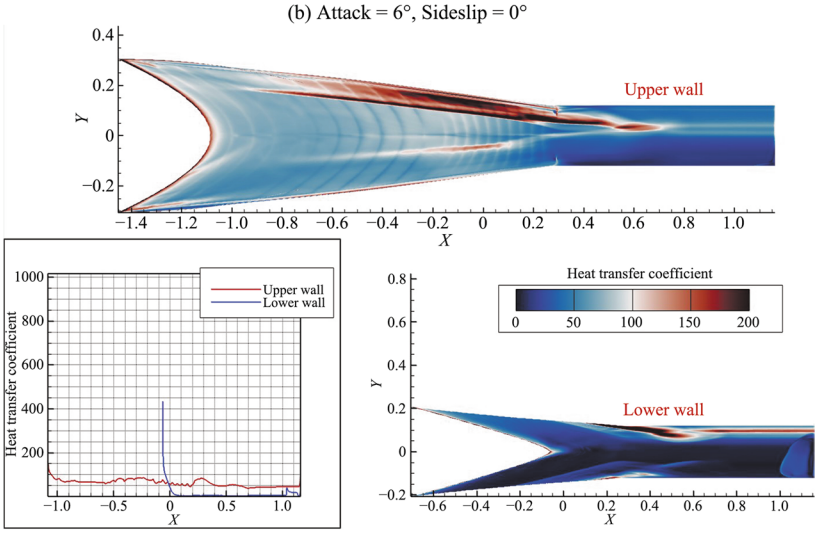

(c) Attack = 6°, Sideslip = 6°

Fig. 7 The heat transfer coefficient contour and curves for the upper and lower walls of the REST inlet

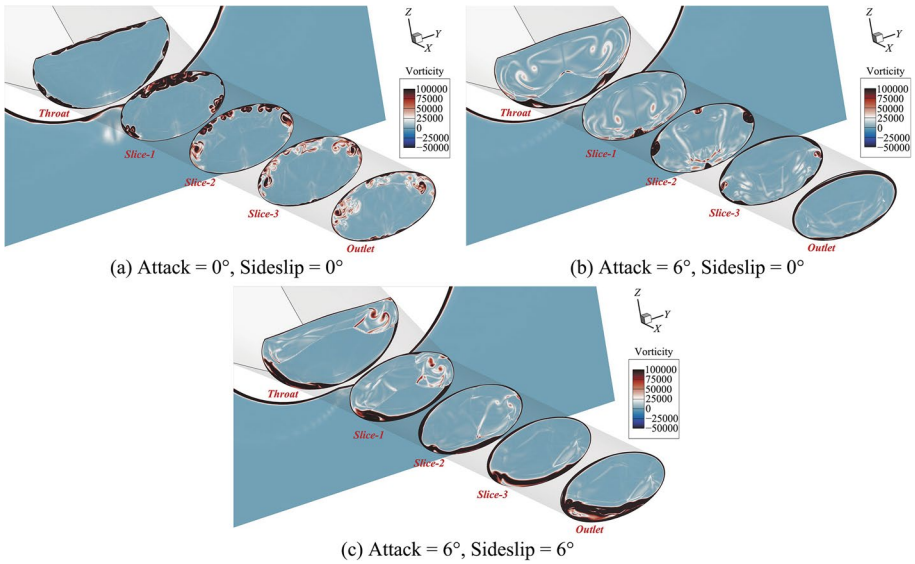

Fig. 8 Vorticity slice contour of the REST inlet

4 Swirl distortion analysis

4.1 Global vorticity

Figure 8 shows the vorticity cross-sections from the throat to the outlet of the REST inlet. The vorticity is a pivotal physical quantity that encapsulates the essence of vortex motion. It is mathematically defined as the curl of the velocity vector. The origin of vorticity within the flow can be attributed to the interaction of the fluid with the solid wall boundary layer, which engenders vortices across a spectrum of sizes. Note that the vorticity is considered as a crucial approach for studying the rotational dynamics across the entire flow field. This approach facilitates the correlation of the turbulent boundary layer within the inlet to the swirl distortion observed at the inlet–outlet.

The vorticity is generated at the throat of the inlet when it is aligned at the design position with Attack and Sideslip of 0°, as shown in Fig. 8a. It is assumed that the boundary layer that lies between the airflow and the transition wall of the inlet is the predecessor of this vorticity. By analyzing the throat section, it can be clearly deduced that the boundary layer at this stage is predominantly a laminar flow, which has yet to encounter the reflected shock wave. This interaction engenders a small-scale vortex structure. The initially laminar boundary layer undergoes a transition to turbulence, with a significant increase in the size and intensity of the vortices, as shown in the slice 1 of Fig. 8a. The formation of large-structured vortices starts upon the interaction of the reflected shock wave at the throat with the boundary layer along the upper wall. These large-structured vortices are then fragmented into smaller entities, and they laterally expand from the upper wall as the flow evolves from slice 1 towards the outlet plane, which verifies the observations presented in Fig. 3a. In addition, it is important to mention that the interaction between the secondary reflected shock waves and the bottom boundary layer results in vortices of reduced size and intensity compared with those arising from the initial shock wave reflections, as shown in slice 3 of Fig. 8a. When the Attack of the incoming flow is altered (Fig. 8b), the shock wave does not attenuate the airflow at the base of the

throat. This can be due to the incident shock wave at the lip, which penetrates into the inlet, creating a substantial velocity gradient against the bottom wall, resulting in significant vorticity. The vortex within the inlet may stem from the transverse pressure differential induced by the incident shock wave at the lip or from the transverse compression of the inlet itself. The vortex at the base of slice 1 is attributed to the interaction between the incident shock wave at the lip and the boundary layer, while the vortices along the sides of the wall in slice 2 are a result of the interaction between the reflected shock wave and the boundary layer. As the flow matures, these vortices disintegrate. In the presence of Attack and Sideslip, the asymmetry of the flow becomes pronounced, as shown in Fig. 8c. It can also be seen from Fig. 3a that at this non-design condition, the reflection of shock waves is not observed. The primary source of the vortex along the bottom wall is identified as the viscous boundary layer, which thickens as the flow progresses. The latter trend is affected by the lateral pressure gradient, responsible for the vortex formation in slices 1 and 2, as well as at the throat.

4.2 Outlet swirl distortion

In this study, an assessment of swirl distortion on the outlet plane of the REST inlet is conducted using a suite of distortion descriptors as outlined in the inlet distortion standard [28, 29], disseminated by the Society of Automotive Engineers (SAE). These descriptors include Swirl Intensity (*SI*), Swirl Directivity (*SD*), and Swirl Pairs (*SP*), which serve as crucial metrics for the characterization of the spatial distribution of swirling motion at the outlet. The quantification of swirl distortion requires measuring the positive (θ_i^+) and negative (θ_i^-) swirl regions within a given ring. In order to perform a comprehensive evaluation, the sector swirl (*SS*) approach is employed for computing the average values of these swirl regions across various measurement rings, which provides a nuanced assessment of the swirl distortion phenomenon.

$$\begin{aligned} SS_{i,k}^{+} &= \frac{1}{\theta_{i,k}^{+}} \int_{\theta_{i,k}^{+}} \alpha(\theta)_{i,k} d\theta, \\ SS_{i,k}^{-} &= \frac{1}{\theta_{i,k}^{-}} \int_{\theta_{i,k}^{-}} \alpha(\theta)_{i,k} d\theta, \end{aligned} \tag{13}$$

where $\alpha(\theta)_{i,k}$ is the swirl angle function of the circumferential location, i is the measurement ring code, and k is the number of low total pressure regions in each measurement ring.

The swirl intensity (*SI*) is the average value of the absolute circumferential swirl angle measured on the ring, which is computed as:

$$SI_i = \frac{\sum_{k=1}^{Q} SS_{i,k}^{+} \cdot \theta_{i,k}^{+} + \sum_{k=1}^{Q} \left| SS_{i,k}^{-} \right| \cdot \theta_{i,k}^{-}}{360}. \tag{14}$$

Equation (15) can be used to determine the Swirl Directivity (*SD*), which is a parameter that is instrumental in characterizing the generalized direction of rotation within a ring, and it ranges between −1 and 1. The *SD* parameter is used to evaluate the swirl

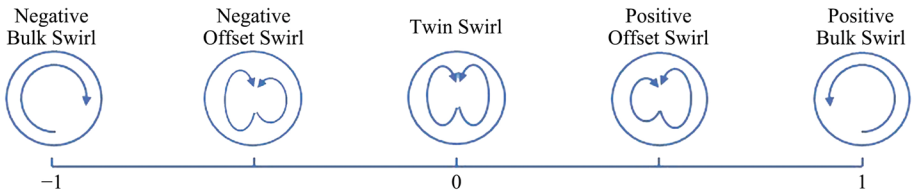

Fig. 9 Descriptor of the swirl directivity distortion

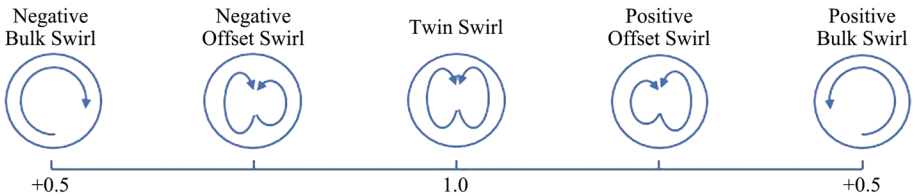

Fig. 10 Descriptor of the swirl pairs distortion

distortion. It allows to quantitatively calculate the rotational tendency. As can be seen in Fig. 9, an *SD* value of −1 indicates the presence of a negative bulk swirl, while a value of 1 indicates a positive one. An *SD* value of 0 denotes the existence of twin swirls within the flow. Furthermore, an *SD* value in the range of −1–0 represents a negative offset swirl. On the contrary, an *SD* value in the range of 0–1 denotes a positive offset swirl, providing a nuanced insight into the details of the swirling flow dynamics.

$$SD_i = \frac{\sum_{k=1}^{Q} SS_{i,k}^{+} \cdot \theta_{i,k}^{+} + \sum_{k=1}^{Q} \left| SS_{i,k}^{-} \right| \cdot \theta_{i,k}^{-}}{\sum_{k=1}^{Q} SS_{i,k}^{+} \cdot \theta_{i,k}^{+} + \sum_{k=1}^{Q} SS_{i,k}^{-} \cdot \theta_{i,k}^{-}}. \tag{15}$$

Equation (16) is employed to determine the quantity of equivalent vortex pairs present within each measurement ring, which is referred to as Swirl Pairs (*SP*). As can be seen in Fig. 10, an *SP* of 0.5 indicates that a single unidirectional vortex exists on the measurement ring. On the contrary, an *SP* of 1 indicates the presence of two vortices of equivalent intensity coexisting on the same ring. Furthermore, an *SP* value between 0.5 and 1 denotes the existence of a pair of vortices on the measurement ring with unequal intensities. This provides a quantitative assessment of the vortex configuration within the flow.

$$SP_i \frac{\sum_{k=1}^{Q} SS_{i,k}^{+} \cdot \theta_{i,k}^{+} + \sum_{k=1}^{Q} \left| SS_{i,k}^{-} \right| \cdot \theta_{i,k}^{-}}{2 \cdot \text{Max of} \left\{ \left[SS_{i,k}^{+} \cdot \theta_{i,k}^{+} \right] \text{or} \left[\left| SS_{i,k}^{-} \cdot \theta_{i,k}^{-} \right| \right] \right\}_{k=1,\ldots,Q}}. \tag{16}$$

It is important to mention that the evaluation descriptors for swirl distortion, initially developed for the assessment of the inlet distortion in turbine engines, are also efficient in capturing the spatially non-uniform distribution of planar swirl

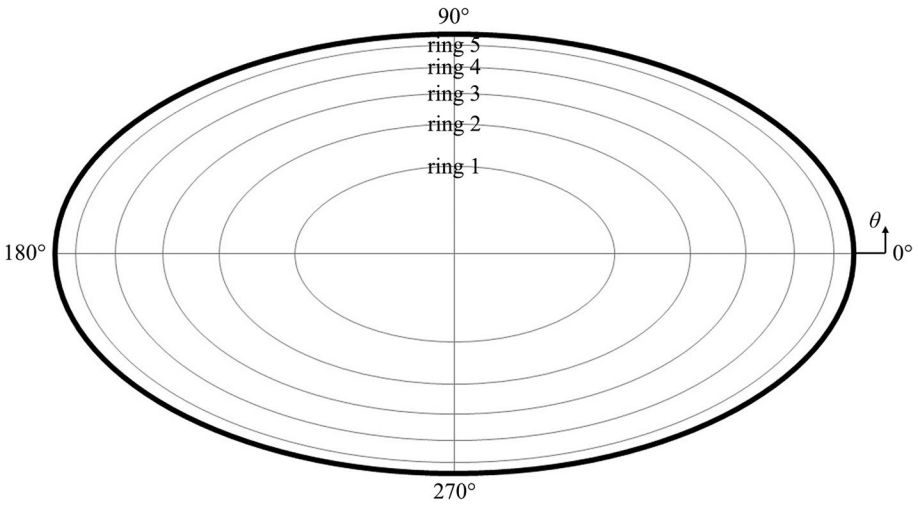

Fig. 11 Distribution of the ring position

characteristics at the circular inlet outlet. Taking into consideration that the REST inlet outlet exhibits an elliptical geometry, this study introduces a more conventional method for defining angular changes and proposes an analogous distortion concept. This concept, grounded in the evaluation descriptor of swirl distortion, as disseminated by the Society of Automotive Engineers (SAE), is employed to evaluate the distortion within the REST inlet under hypersonic flow conditions. Figure 11 shows the spatial arrangement of the five measuring rings on the outflow plane. The radial positions of these rings, denoted by (r_i), are related to the outermost ellipse (r_0), with proportions of $r_i/r_0 = 0.40$, 0.59, 0.73, 0.85, and 0.95.

Figure 12 shows the distribution of the time-averaged swirl angle across the circumferential locations of the five measuring rings, allowing to more clearly highlight the magnitude of the swirl angle and its spatial impact. In the case where both the Attack and the Sideslip are set to 0°, the swirl angles across the five rings shown in Fig. 12a are minimal, ranging between −3° and 3°. Although these small angles exist, each ring fluctuates with a different intensity, and the amplitude of these fluctuations linearly increases with the increase of the ring radius. Ring 5 indicates the presence of two swirl pairs on the outlet plane. At the non-design condition, defined by a Sideslip of 0° and an Attack of 6° (Fig. 12b), the inner four measuring rings exhibit negligible variation in the swirl angle. However, ring 5 exhibits a significant swirl angle variation at the circumferential position of 270°, which demonstrates the influence of a strong swirl pair with an extensive impact radius. On the contrary, it can be seen from Fig. 12c that no significant difference in the swirl angle exists between the cases with a Sideslip of 0° and an Attack of 6° for the first two rings. However, the outer rings, specifically rings 3, 4, and 5, exhibit an alternating distribution of swirl angles within the angular range of 180°–300°. This indicates more complex flow dynamics in these regions. These results are consistent with the outlet plane effects illustrated in Fig. 8c.

In this study, the inlet distortion descriptors are derived by applying two different methodologies. The first approach, which is based on the temporal averaging of the swirl angle, yields the descriptors that comprise the time-averaged distortion characteristics.

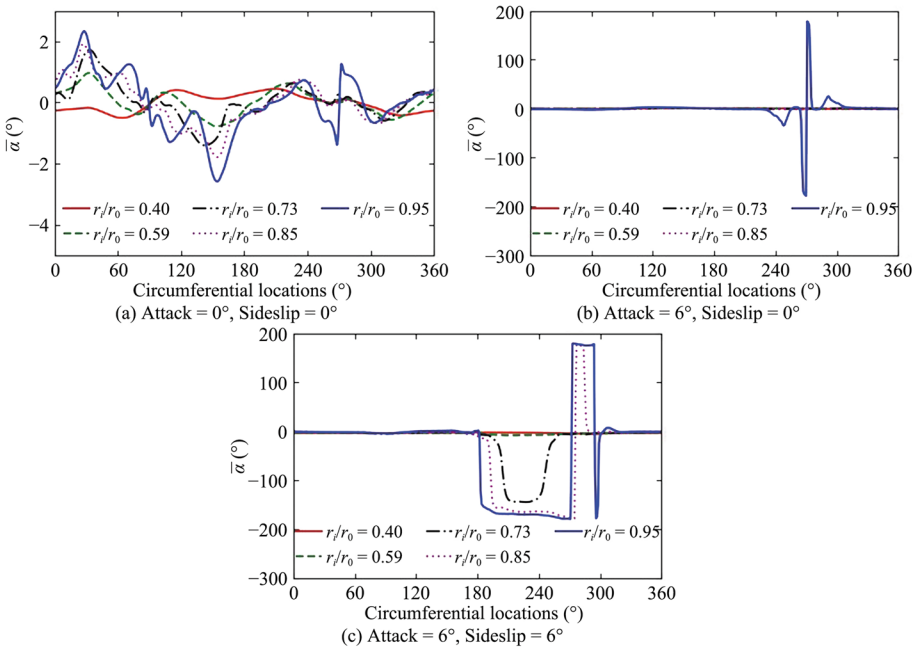

Fig. 12 Distribution of the time-averaged swirl angle at the circumferential position of the five measuring rings

The second technique involves the computation of the distortion descriptors from the instantaneous values, followed by their arithmetic averaging for capturing the average effect of instantaneous distortion. The results of these computations are shown in Fig. 13. In particular, the calculations yielding the results of Fig. 13a, b, and c are based on the time-averaged swirl angle, while those of Fig. 13d, e, and f are based on the instantaneous swirl angle. It can be seen from Fig. 13a that the time-averaged swirl intensity across the five measuring rings converges to zero at the design condition, where both the Attack and the Sideslip are set to 0°. At the non-design condition with 6° Attack and 0° Sideslip, the time-averaged swirl intensity at ring 5 is slightly increased above the design point. However, a significant increase in the time-averaged swirl intensity is observed for rings 3, 4, and 5 when both the Attack and the Sideslip are increased to 6°. This indicates that the joint effect of the Attack and Sideslip significantly amplifies the swirl intensity. It can be observed from Fig. 13b that the time-mean swirl directivity assumes negative values at the non-design condition of 6° Attack and 6° Sideslip, with negligible variations at the other two design conditions. The variations of the pulsating swirl intensity, shown in Fig. 13a and d, mirror those of the time-averaged swirl intensity, with greater magnitudes. A distinct change in the direction of the pulsating swirl is observed at the design point with Sideslip and Attack of 0°, as shown in Fig. 13e. An analysis of the computed values demonstrates that there is no statistically significant difference between the time-averaged swirl angle-based descriptors and the mean values of the pulsation swirl distortion descriptors. However, it can be clearly seen that the swirl distortion descriptors are more pronounced at non-design conditions (in particular, under 6° Attack and 6° Sideslip), which demonstrates the increase of the degree of swirl distortion with the increase of the Attack and Sideslip at these conditions.

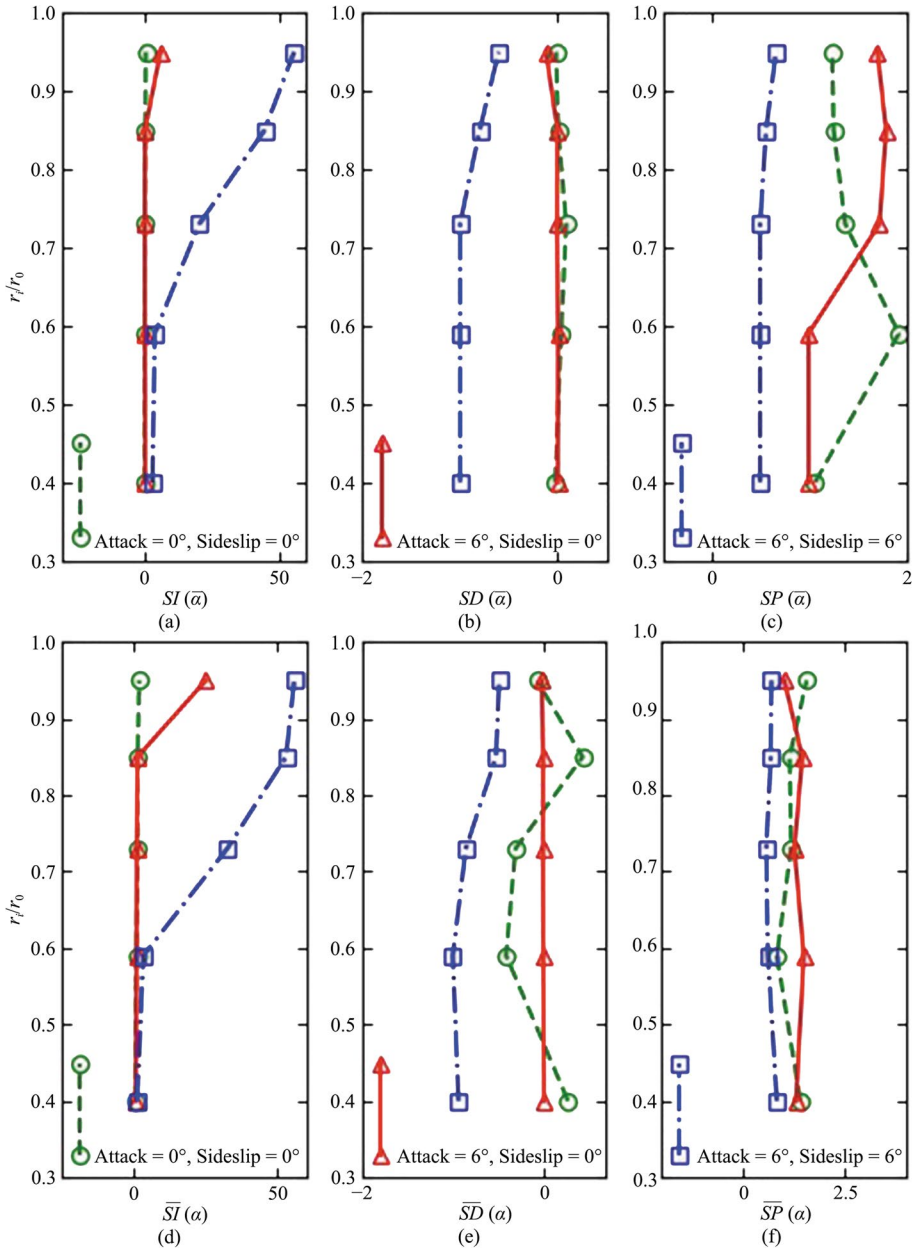

Fig. 13 Descriptors of the swirl distortion

5 Conclusions

This study uses the Large Eddy Simulation (LES) method to comprehensively analyze the flow field characteristics of the REST inlet at Mach 6 conditions, including instantaneous flow characteristics, time-averaged flow characteristics, and swirl distortion at the outlet plane. It summarizes the influence of the shock wave-turbulence interaction on the outlet swirl distortion, and explores the flow characteristics under design and off-design conditions.

At the design point (0° Attack and 0° Sideslip), the incident shock wave at the inlet lip reflects multiple times within the inlet and interacts with the reflected shock waves in the domain wall boundary layer, forming turbulent structures. The first reflected shock wave has the highest energy and the most significant impact on the boundary layer,

which results in the formation of large-scale vortex structures. However, due to the multiple reflections of the incident shock wave, its energy gradually decreases, which results in decreasing the swirl distortion at the outlet.

Under off-design conditions, such as 6° Attack and 0° Sideslip, as well as 6° Attack and 6° Sideslip, the change of the incoming flow conditions causes the incident shock wave to move inward, which decreases its reflection frequency and also removes the reflection shock waves under the conditions of 6° Attack and 6° Sideslip. However, the swirl angle and distortion intensity at the outlet significantly increase. This demonstrates that the change of the incoming flow conditions affects the degree of swirl distortion at the outlet by affecting the shock wave-turbulence interaction, the position of the incident shock wave, and the number of reflected shock waves.

A numerical simulation of the REST inlet is then conducted. The obtained results demonstrate the intrinsic connection between shock wave-turbulence boundary layer interaction and swirl distortion. They also describe the impact of the shock wave-turbulence interaction on the outlet swirl distortion. The findings of this study are of great significance for understanding and predicting the performance of hypersonic inlets under various flight conditions, and guiding the design and optimization of inlets.

Furthermore, this study analyzes the wall heat transfer coefficient of the inlet. The obtained results show that the shock wave-boundary layer interaction significantly affects the heat transfer coefficient. Considering these factors during the design process is also crucial for increasing the thermal protection ability and the overall performance of the inlet.

In summary, this study allows to better understand the flow field characteristics of hypersonic inlets, and provides theoretical support and technical guidance for the design and performance optimization of inlets. In future work, this study will be expanded to tackle the reduced-order models.

Nomenclature

REST	Rectangular-to-Elliptical Shape Transition
dS	The closed surface of integral
F_{inv}	Inviscid flux vector
F_{vis}	Viscous flux vector
W	Conserved variable vector
W_L	The left solution vector
W_R	The right solution vector
δW	Spatial difference
WALE	Wall-Adapting Local Eddy-Viscosity
μ_t	Eddy viscosity coefficient
α	Swirl angle
SI	Swirl Intensity
SD	Swirl Directivity
SP	Swirl Pairs
SAE	Society of Automotive Engineers
SS	Sector Swirl

Acknowledgements
Not applicable.

Authors' contributions
ZW was responsible for analyzing the experimental data and drafting the initial version of the manuscript, as well as revising subsequent versions. YL oversaw the experimental procedures and authored the manuscript throughout the project. LL provided technical guidance during numerical simulations. XX and RL handled the data processing component of the manuscript. All authors read and approved the final manuscript.

Funding
This research was funded by the National Natural Science Foundation of China (Grant No. 12002144) and the Jiangxi Provincial Natural Science Foundation (Grant No. 20212BAB211015).

Availability of data and materials
The datasets generated and/or analyzed during the current study are not publicly available, but are available from the corresponding author on reasonable request.

Declarations

Competing interests
The authors declare that they have no competing interests.

Received: 27 February 2024 Accepted: 14 June 2024
Published online: 08 October 2024

References

1. Smart MK (2010) Scramjet inlets. In: High speed propulsion: Engine design-integration and thermal management (RTO-EN-AVT-185). NATO Research and Technology Organization, Brussels
2. Van Wie DM, Kwok FT, Walsh RF (1996) Starting characteristics of supersonic inlets. In: 32nd joint propulsion conference and exhibit, Lake Buena Vista, 1-3 July 1996. https://doi.org/10.2514/6.1996-2914
3. Molder S, Romeskie JM (1968) Modular hypersonic inlets with conical flow. AGARD Conf Proc 30:9
4. Billig FS (1995) Supersonic combustion ramjet missile. J Propul Power 11(6):1139–1146. https://doi.org/10.2514/3.23952
5. Smart MK (1999) Design of three-dimensional hypersonic inlets with rectangular-to-elliptical shape transition. J Propul Power 15(3):408–416. https://doi.org/10.2514/2.5459
6. Hartill WB (1965) Analytical and experimental investigation of a scramjet inlet of quadriform shape (US Air Force TR AFAPL-TR-65-74). Marquardt Corporation, Los Angeles
7. Fuller EJ (1992) Experimental and computational investigation of helium injection into air at supersonic and hypersonic speeds. Dissertation, Virginia Polytechnic Institute and State University
8. Smart MK, Trexler CA (2004) Mach 4 performance of hypersonic inlet with rectangular-to-elliptical shape transition. J Propul Power 20(2):288–293. https://doi.org/10.2514/1.1296
9. Smart MK (2001) Experimental testing of a hypersonic inlet with rectangular-to-elliptical shape transition. J Propul Power 17(2):276–283. https://doi.org/10.2514/2.5774
10. Schulte D, Henckels A, Neubacher R (2001) Manipulation of shock/boundary-layer interactions in hypersonic inlets. J Propul Power 17(3):585–590. https://doi.org/10.2514/2.5781
11. Xie WZ, Wu ZM, Yu AY et al (2018) Control of severe shock-wave/boundary-layer interactions in hypersonic inlets. J Propul Power 34(3):614–623. https://doi.org/10.2514/1.B36614
12. Xu S, Wang Y, Wang Z et al (2022) Experimental investigations of hypersonic inlet unstart/restart process and hysteresis phenomenon caused by angle of attack. Aerosp Sci Technol 126:107621. https://doi.org/10.1016/j.ast.2022.107621
13. Zhai J, Zhang CA, Wang FM et al (2022) Control of shock-wave/boundary-layer interaction using a backward-facing step. Aerosp Sci Technol 126:107665. https://doi.org/10.1016/j.ast.2022.107665
14. Saad MR, Zare-Behtash H, Che-Idris A et al (2012) Micro-ramps for hypersonic flow control. Micromachines 3(2):364–378. https://doi.org/10.3390/mi3020364
15. Mogrekar A, Sivakumar R (2014) CFD analysis of micro-ramps for hypersonic flows. Appl Mech Mater 592-594:1962–1966. https://doi.org/10.4028/www.scientific.net/AMM.592-594.1962
16. Gupta G, Ashok Kumar A, Sivakumar R et al (2022) CFD investigation of shock boundary layer interaction in hypersonic flow and flow control using micro ramps. Aircr Eng Aerosp Technol 94(6):862–870. https://doi.org/10.1108/AEAT-04-2020-0069
17. Zhang Y, Tan HJ, Zhuang Y et al (2014) Influence of expansion waves on cowl shock/boundary layer interaction in hypersonic inlets. J Propul Power 30(5):1183–1191. https://doi.org/10.2514/1.B35090
18. Meshram S, Siva V, Peetala RK (2019) Shock wave boundary layer interaction (SWBLI) in hypersonic flow over a blunt body double wedge configuration. J Phys Conf Ser 1276(1):012005. https://doi.org/10.1088/1742-6596/1276/1/012005
19. Zahrolayali N, Saad MR, Che Idris A et al (2022) Assessing the performance of hypersonic inlets by applying a heat source with the throttling effect. Aerospace 9(8):449. https://doi.org/10.3390/aerospace9080449
20. Guo T, Zhang J, Tong F et al (2023) Amplification of turbulent kinetic energy and temperature fluctuation in a hypersonic turbulent boundary layer over a compression ramp. Phys Fluids 35(4):046118. https://doi.org/10.1063/5.0145320
21. Zhu K, Xie F, Wang G et al (2023) Separation characteristics of shock wave/turbulent boundary layer interaction under the effect of a transverse jet. Phys Fluids 35(5):055142. https://doi.org/10.1063/5.0148359

22. Emami S, Trexler CA, Auslender AH et al (1995) Experimental investigation of inlet-combustor isolators for a dual-mode scramjet at a Mach number of 4 (NASA-TP-3502). NASA Langley Research Center, Hampton
23. Ombrello T, Peltier S, Carter CD (2015) Effects of inlet distortion on cavity ignition in supersonic flow. In: 53rd AIAA aerospace sciences meeting, Kissimmee, 5-9 January 2015. https://doi.org/10.2514/6.2015-0882
24. Li Y, Wu Z, Wu S et al (2023) Assessment of total pressure and swirl distortions in a Busemann inlet at Mach 6. J Appl Fluid Mech 16(9):1865–1876. https://doi.org/10.47176/JAFM.16.09.1749
25. Geurts BJ, Kuerten JGM, Vreman AW et al (1993) A finite volume approach to compressible large eddy simulations. In: Nieuwstadt FTM (eds) Advances in turbulence IV. Fluid mechanics and its applications, vol 18. Springer, Dordrecht. https://doi.org/10.1007/978-94-011-1689-3_52
26. Zhang Y, Zhang L, He X et al (2017) Detached eddy simulation of complex separation flows over a modern fighter model at high angle of attack. Commun Comput Phys 22(5):1309–1332. https://doi.org/10.4208/cicp.OA-2016-0132
27. Kinefuchi K, Starikovskiy AY, Miles RB (2018) Numerical investigation of nanosecond pulsed plasma actuators for control of shock-wave/boundary-layer separation. Phys Fluids 30(10):106105. https://doi.org/10.1063/1.5051823
28. SAE International (2017) Inlet total-pressure-distortion considerations for gas-turbine engines (AIR1419C). SAE International, Warrendale. https://doi.org/10.4271/AIR1419C
29. SAE International (2017) A methodology for assessing inlet swirl distortion (AIR5686). SAE International, Warrendale. https://doi.org/10.4271/AIR5686

Publisher's Note